Tensile behaviour of uncured Sheet Moulding Compounds: rheology and flow-induced microstructures

8 authors, including:

Thibaud Cochereau
University Joseph Fourier - Grenoble 1
4 PUBLICATIONS **8** CITATIONS

SEE PROFILE

Laurent Orgéas
French National Centre for Scientific Research
168 PUBLICATIONS **1,499** CITATIONS

SEE PROFILE

Sabine Rolland du Roscoat
University Joseph Fourier - Grenoble 1
72 PUBLICATIONS **611** CITATIONS

SEE PROFILE

Some of the authors of this publication are also working on these related projects:

Project — Rheology of concentrated fibre suspensions View project

Project — Multiphysical simulation in composites forming processes View project

Tensile behaviour of uncured sheet moulding compounds: Rheology and flow-induced microstructures

CrossMark

D. Ferré Sentis [a,b,c], T. Cochereau [a], L. Orgéas [a,*], P.J.J. Dumont [b], S. Rolland du Roscoat [a], T. Laurencin [a,b], M. Terrien [d], M. Sager [c]

[a] Univ. Grenoble Alpes, CNRS, Grenoble INP, 3SR Lab, F-38000 Grenoble, France
[b] Univ. Lyon, INSA-Lyon, CNRS UMR5259, LaMCoS, F-69621, France
[c] Plastic Omnium Auto Exterior, Sigmatech, F-01150 Sainte Julie, France
[d] Univ. Grenoble Alpes, CNRS, Grenoble INP, LGP2, F-38000 Grenoble, France

ABSTRACT

During compression moulding, Sheet Moulding Compounds (SMCs) are subjected to tensile strains that yield detrimental tears. To understand these mechanisms, tensile experiments were performed with two uncured industrial SMC formulations with low and high pore and fibre contents. These experiments were coupled with Digital Image Correlation to estimate mesoscale strain fields on the sample surface. X-ray microtomography was used to obtain 3D *ex situ* evolutions of pores and fibre-bundle orientation. Both formulations behaved as porous, elastoviscoplastic, anisotropic and shear thinning fluids, showing strain hardening followed by softening and sample breakage. During stretching, SMCs dilated with anisotropic pore growth, whereas fibre bundles aligned along the tensile direction following the prediction of the modified Jeffery's equation. In addition, the ductility of SMCs was largely altered both by the initial pore contents and fibre-bundle flocs/aggregates induced during the prepreg fabrication, the latter leading to undesirable strain localisation bands enhancing sample breakage.

© 2017 Elsevier Ltd. All rights reserved.

1. Introduction

Sheet moulding compounds (SMC) are thermoset prepregs that are widely used in the automotive, aeronautics and electrical industries. They exhibit excellent properties for a reasonable cost and weight. SMCs are composed of a thermoset filled matrix (polyester, vinylester, epoxy) reinforced with 15–60 wt% of chopped fibres or fibre bundles with a typical length that ranges between 10 and 50 mm (glass or carbon fibre bundles, biosourced fibres). Before their forming, these materials are prepared in the form of prepregs, *i.e.*, 1 to 3-mm thick sheets [1]. The fabrication process is achieved by compression moulding which can often be divided into four steps: (i) a stamping phase of the SMC charges to make them roughly fit the complex shapes of the moulds to be filled, (ii) a compression phase corresponding to the mould closure, (iii) a curing phase of the thermoset matrix, and (iv) an ejection of the produced part. The two first steps involve complex flow mechanisms, drastic and not well-predicted evolutions of the SMC microstructures that can be at the origin of critical defects affecting the end-use properties of produced parts [2–8].

During the stamping phase, SMCs are subjected to in-plane tensile and shear loadings, out-of-plane bending, transverse tension–compression and shear similarly to other thermoformed thermoplastic prepregs or dry fabrics. In particular, in-plane tensile deformation modes can cause undesirable porosities and tears in the SMC charges. This kind of damage is illustrated in Fig. 1a–b. In addition, during the compression phase, the flow of SMC layers often proceeds as plug flow, *i.e.*, each individual sheets being mainly subjected to an in-plane extension [3,6,7,9]. At the SMC flow front, where the inner SMC layers can be squished out [6], as well as inside vertical zones of the mould, the SMC in-plane extension occurs with low or without compressive isostatic stresses, *i.e.*, close to tensile stress states. This can also generate detrimental pores and tears of the SMC charges, as emphasized in Fig. 1c–d.

So far, numerous studies have focused on the rheology of SMCs under compressive or shear deformation modes, using dedicated large rheometers due to the non negligible fibre length [5,10–20]. Astonishingly, despite the commonly observed defects induced by SMC stretching (Fig. 1), very few studies investigated the tensile

---

* Corresponding author.
  E-mail address: Laurent.Orgeas@3sr-grenoble.fr (L. Orgéas).
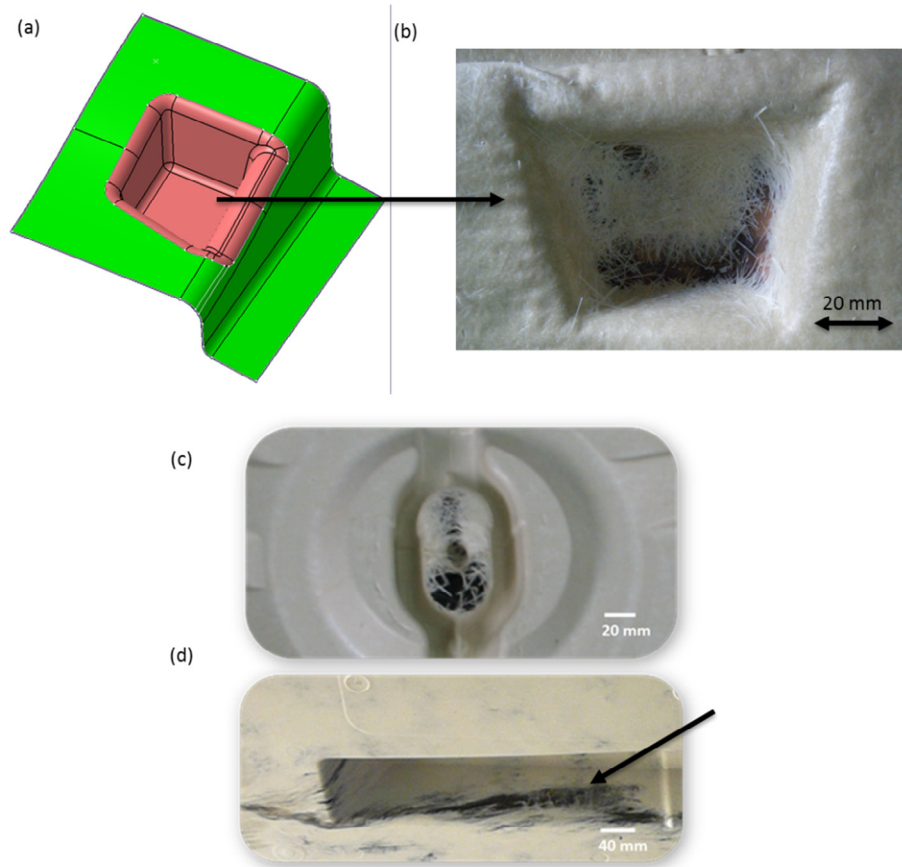
Fig. 1. Typical SMC tears observed during the stamping phase (a) or the compression phase (c–d). In (d), the SMC tearing that occured in a vertical zone of the mould has been highlighted using initial SMC charges with stacks of sheets with cream and black colors. (For interpretation of the references to colour in this figure legend, the reader is referred to the web version of this article.)

behaviour of SMCs [10]. In their pioneering work, Lee et al. [10] only reported some trends. The studied SMCs exhibited a low deformability, *i.e.*, they could only be elongated about 5% before failure. The authors also observed the relative motion between fibre bundles and their pull-out from the SMC matrix at the sample surface. Those qualitative observations are interesting. However, they are insufficient to properly understand and model the mechanics of SMC in tension and to avoid SMC tears during the compression moulding process. This study provides neither quantitative data on the tensile rheology of SMC nor on the tensile-induced evolutions of the SMC microstructures, *e.g.*, on the pore growth and fibre bundle kinematics induced during the SMC stretching. Thus, it is important to characterise the tensile properties of SMC prepregs. This would allow proposing guidelines for constitutive models implemented in simulation codes so as to avoid SMC residual pores and tears during compression moulding.

To this end, it is interesting to notice that the tensile behaviour of other dry or impregnated woven fabrics, as well as other disordered fibrous materials such as papers or non-woven fibrous mats has been extensively studied using either uniaxial or biaxial loading conditions. For ordered structures with continuous fibres such as woven fabrics, most of these studies were dedicated to the analysis of (i) the mechanical behaviour along the fibre directions, *e.g.* to analyse the unfolding and the breakage of yarns, (ii) the in-plane shear of the textiles, conducting the so-called bias-extension tests [21–23]. As both the mechanics and the microstructures of these fibrous architectures are very different from those of SMCs, it is difficult to extrapolate from these studies information on the tensile behaviour of SMCs, apart from technical information related to

the experimental procedure. For instance, using Digital Image Correlation DIC techniques [24], Cao *et al.* [22] showed that very useful information on the kinematical fields on the surface of woven samples could be obtained during bias-extension tests. In parallel, interesting studies deal with the mechanics and the microstructures of soft entangled fibre networks [25,26], papers [27–31] and non-woven materials [32–34] during uniaxial extension tests. The use of DIC was also very useful to analyse the local kinematic fields on the surface of deformed samples [28,31–33]. These studies also provided interesting guidelines to understand the mechanics of these fibrous networks and to link their behaviour to the evolution of their microstructures. For example, by combining tensile tests and 3D *in situ* observations using X-ray microtomography, Rodney *et al.* linked the macroscale auxetic (in tension) and dilatant (in compression) behaviour of entangled single wire materials with their fibrous architecture (fibre orientation, curvature and connectivity). However, none of the aforementioned entangled and disordered fibrous systems were impregnated with a non-Newtonian polymer matrix as SMCs. As already observed in these systems [5,10–20], this matrix can have large effects on the macroscale tensile behaviour and the evolution of the flowing microstructures (fibre orientation, pore growth).

Thus, the main objective of this study is to bring an exhaustive analysis of the tensile rheology as well as the related evolving microstructures of two industrial SMC formulations, having a standard fibre content and a moderate porosity, and a high fibre content and porosity, respectively. Among the questions to be elucidated, the followings are addressed herein: does the macroscale tensile behaviour of SMCs exhibits similarities with other

loading modes such as compression or shear? What are the SMC tensile ductility, the strain rate sensitivity? What are the roles of the fibre content and spatial distribution on mesoscale strain fields upon stretching SMCs? What are the pore growth and fibre orientation evolutions? For that purpose, a tensile test setup was designed, enabling the macroscale strains fields to be recorded during the experiments using DIC. This device could be mounted in a laboratory X-ray microtomograph so that *ex situ* analysis of the evolution of the microstructures of SMC samples could be performed at different stages of deformation.

2. Materials, tools and methods

2.1. Materials

The samples were extracted from two typical industrial formulations of SMC with two very different fibre contents. SMCs were fabricated by MCR – Plastic Omnium (Tournon-sur-Rhône, France) and were identical to those recently studied [20]. The first SMC formulation, denoted *S*, was composed of a polyester-based paste reinforced with 29 wt% of glass fibre bundles with a length of 25 mm, height ≈ 0.05 mm and width ≈ 0.5 mm. This formulation is typically used to produce lightweight automotive semi-structural parts. Its macroscale rheology is similar to that of several standard SMC formulations that were previously studied [16,17]. The second SMC formulation, denoted *H* in the following sections, was a vinylester-based paste reinforced with 50 wt% glass fibre bundles having the same dimensions as the *S* formulation. This SMC is used to manufacture automotive structural parts. Tensile specimens were cut from the middle zones of sheets [35] in the shape of slender rectangles of dimensions $l_0 w_0 = 400 \times 50$ mm^2 parallel (*MD*) and perpendicular (*CD*) to the machine direction. Their initial thicknesses t_0 were equal to 2 and 3 mm for the *S* and *H* specimens, respectively. Their initial fibre volume fractions were close to 0.22 and 0.27, respectively.

2.2. Standard tensile tests

An electromechanical tension–compression machine (Fig. 2a) was used to conduct the uniaxial tensile tests (MTS 4M, max. load 20 kN, max stroke velocity 15 mm s^{-1}). The compression device was equipped with a load cell of 500 N to record the tensile force F_1 and to calculate the nominal tensile stress $\sigma_{11} = F_1/(t_0 w_0)$, from

the knowledge of the initial sample width w_0 and thickness t_0. The clamps used to grip samples were covered with sandpaper in order to avoid sample slipping. The initial gauge length between the clamps was set to $h_0 \approx 300$ mm. During tensile tests, the actual height h of the sample was measured from the displacement of the cross-head of the machine, enabling the mean tensile Hencky strain $\bar{\varepsilon}_{11} = \ln(h/h_0)$ to be measured. Before testing, note that samples were subjected to a small tensile stress (3.10^{-3} MPa) to ensure that they were not bent. After the relaxation of this stress (≈ 3 min), the mechanical loading was applied. It consisted in stretching samples at constant mean strain rate $\bar{D}_{11} = \dot{h}/h$ along the $\mathbf{e}_1$-direction up to failure. Strain rates $\bar{D}_{11}$ that ranged from 10^4 s^{-1} to 10^1 s^{-1} were used, including values encountered during the SMC process. For each of the testing conditions, tests were performed at least three times.

In order to estimate the local strain field on the surface of stretched samples and to avoid potential slipping of samples in the clamps, a DIC setup was coupled to the tensile device using (i) a CCD camera (Jai Pulnix, spatial resolution of 1624 × 1236 pixels, frame rate of 10 Hz, Fig. 1a), and (ii) the 7D DIC software [24,31]. Hence, before testing, samples were coated with spray-paint speckles. We checked that the speckles did not modify the mechanical response of the samples. For the *H* formulation (Fig. 1b), a black spraypaint was directly sprayed onto the sample surface, whereas, for the *S* formulation (Fig. 1c), a uniform white layer was firstly used before applying the black spaypaint layer. The correlation analysis was conducted with correlation grid steps and windows of equal sizes set to 20 × 20 pixels. Thus, it was possible to obtain 2D maps of the local Hencky strain tensor $\boldsymbol{\varepsilon}$ on the sample surfaces.

Uniaxial and lubricated compression tests along the $\mathbf{e}_3$-direction were also performed at various and constant compression strain rates $\bar{D}_{33}$ to show similarities with results obtained in tension. For that purpose, the experimental procedure reported in [16,17] was used: cylindrical stacks of two SMC layers with a diameter $D_0 = 80$ mm were lubricated and compressed inside a compression rheometer, and the SMC nominal stress at the onset of the SMC flow $\sigma_{33} = 4F_3/\pi D_0^2$ was recorded.

2.3. Ex situ tensile setup for 3D imaging

To link the macroscale tensile behaviour of SMCs with their microstructures, two additional tensile tests were also performed

(a)   (b)   (c)
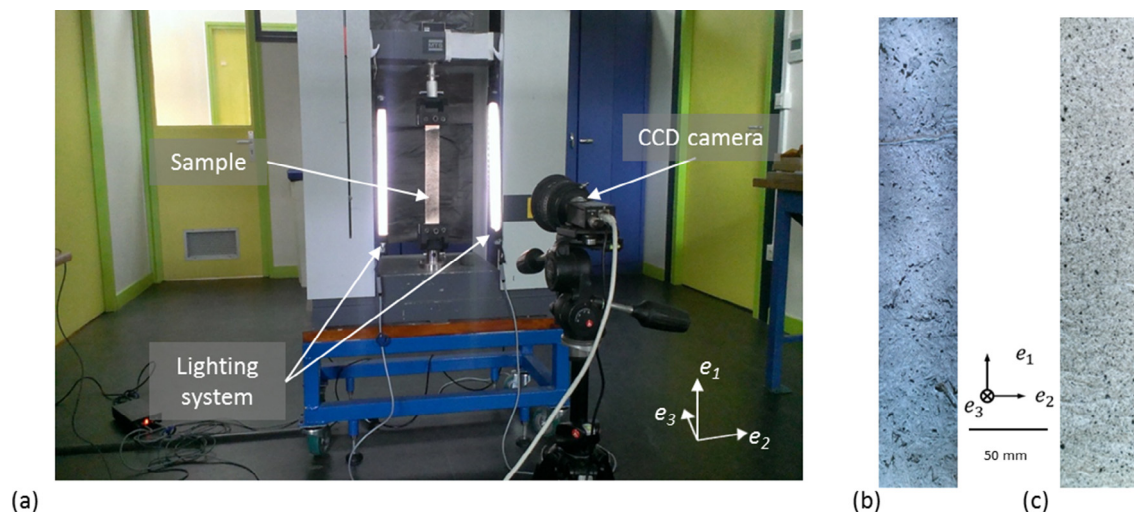
Fig. 2. Experimental setup showing the tension–compression machine, a sample mounted in the tensile clamps, the lighting system and the CCD camera used for DIC experiments used to estimate the Hencky strain tensor $\boldsymbol{\varepsilon}$ on the surface of the sample (a). Photographs of the *S* (b) and *H* (c) samples showing the speckles on the surface of SMC samples. (For interpretation of the references to colour in this figure legend, the reader is referred to the web version of this article.)

with one S and one H sample, using a specially designed tensile setup (Fig. 3a). Compared with the standard setup shown in Fig. 2, the new setup was equipped with a transparent cylindrical chamber made of PMMA. This chamber could also enabled the stretching of the sample to be recorded with the video camera and the DIC analysis to be achieved properly. The tensile tests consisted in stretching the specimens at constant strain rate $\bar{D}_{11} = 5.10^{-3} \text{ s}^{-1}$ up to a given tensile strain, after which a relaxation was carried out up to full stress relaxation. This operation was repeated several times (e.g. seven times for the S sample and 3 times for the H sample). For four stages denoted ①,②,③,④ in the following sections, the test was temporally interrupted by fixing the relaxed sample configuration with locking screws (Fig. 3a). Then, the setup was mounted on the rotation stage of a laboratory X-ray microtomograph (3SR Lab, Grenoble, France, RX solutions) in order to perform a complete scan of the sample (Fig. 3b). For that, 1500 radiographs of the sample were acquired over a 360° rotation of the sample (X-ray voltage: 86 kV, current intensity: 300 μA) with a voxel size of $45 \times 45 \times 45$ μm^3. As the sample height was larger than the X-ray detector height, 5 scans per sample were required (total scanning time of approximately 2 h). The resulting images were concatenated to obtain, after reconstruction, full 3D grey-level images, representing the X-ray absorption coefficient of the samples.

2.4. Image analysis

From the 3D images, various image analysis procedures were carried out to analyse both the shape of deformed samples and extract descriptors of their microstructure. These analyses were done using the softwares Fiji and Matlab. Some of them are identical to those reported in a previous study [20]:

– Using the function "Wand" of Fiji, the mean in-plane area $\bar{A}$ (in the $(\mathbf{e}_1, \mathbf{e}_2)$ plane) of samples between the clamps was estimated. This allowed the mean sample surface strain $\bar{\varepsilon}_s = \ln(\bar{A}/\bar{A}_0)$ to be calculated [20].
– The good contrast between the pores and the solid phases of imaged samples enabled easy manual thresholding operation. After filling the closed pores, the volumes V of the samples were

calculated by counting the number of voxels that constituted the sample. Then, the mean volumetric strain $\bar{\varepsilon}_v = \ln(V/V_0)$ was calculated for each deformed and imaged sample.

– As fibre bundles exhibited planar orientation, their orientation was estimated using the plugin OrientationJ [36]. This plugin is based on the estimation of the gradients in a region of interest (ROI) of 2D grey scale images, from which 2D structure tensors $\mathbf{A}_i$ within the neighbourhood of N pixels i in the ROI are built. Then, structure tensors $\mathbf{A}_i$ were averaged in the fibrous phase of the ROI (as shown in Fig. 3a and c) to build a mean second order fibre orientation tensor $\mathbf{A}$ [37]:

$$\mathbf{A} = \frac{1}{N}\sum_N \mathbf{A}_i, \tag{1}$$

This tensor was computed $\mathbf{A}$ by averaging its values for all the slices of a 3D image. We also checked that the components of this tensor were consistent with those obtained using manual measurements [38,39].

– Other image analysis operations were also performed with segmented images (Fig. 4) that were obtained after manual thresholding. These analyses were achieved in the ROIs shown in Fig. 4. Thus, various microstructural descriptors of the porous phase such as the volume fraction of pores ϕ_p, the 2D mean in-plane porosity $\bar{\phi}_{p2D}$ and the pore anisotropy ratios r_{12}, r_{13} and r_{23} (deduced from the calculation of the mean chord lengths in the porous phase) were computed using procedures extensively reported in [20].

3. Results

3.1. Typical macroscale results

The principal macroscale observations deduced from the tensile tests coupled with DIC and tomography are shown in Figs. 5–7. Fig. 5 shows two typical stress–strain curves and strain maps and paths (deduced from the DIC) obtained after stretching (or compressing) at constant strain rate (with or without stress relaxation) two S and H samples. Fig. 6a provides some photographs of several
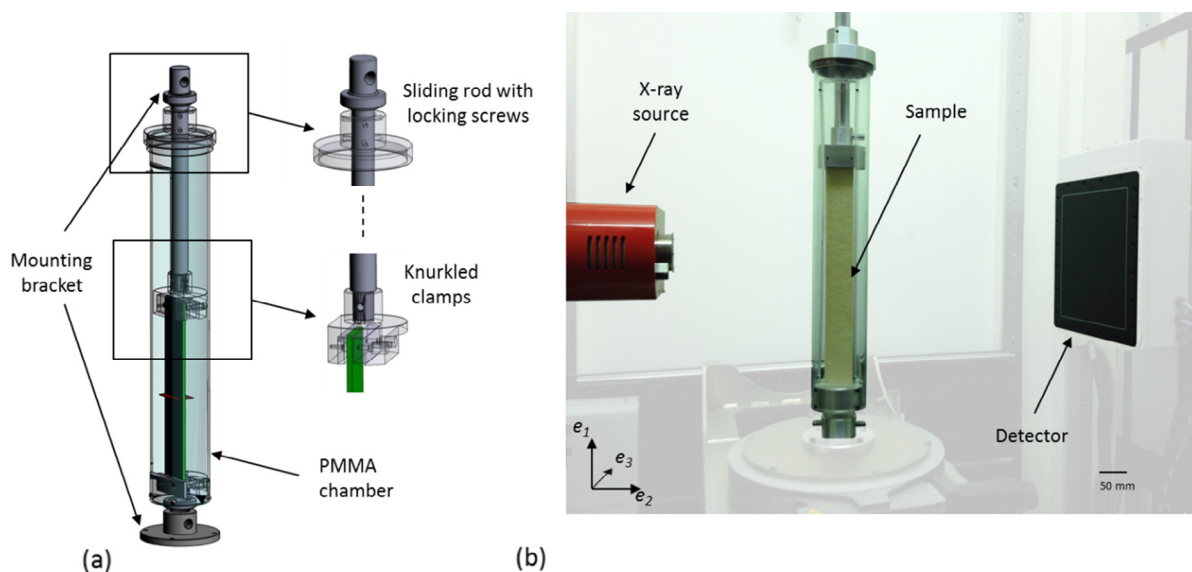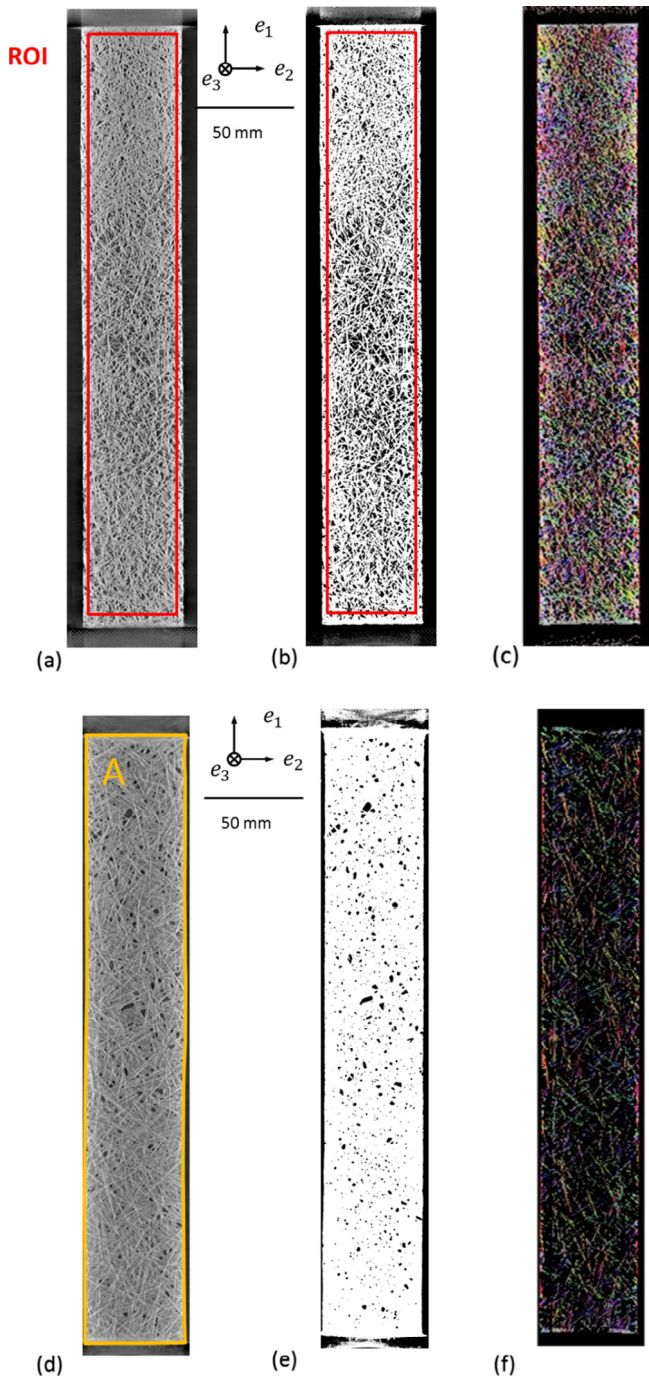

Fig. 3. Detailed view of the designed chamber used for the 3D *ex situ* imaging experiments (a), and view of the setup once mounted in the X-ray microtomograph (b, 3SR Lab, Grenoble, France). (For interpretation of the references to colour in this figure legend, the reader is referred to the web version of this article.)

Fig. 4. Initial grey scale slices (a, d), slices segmented on the pores phase (b, e, black), and orientation maps obtained using orientationJ (c, f) for the *S* (a–c) and the *H* (d-f) samples. (For interpretation of the references to colour in this figure legend, the reader is referred to the web version of this article.)

S and *H* samples after breakage, as well as some trends about the influence of the strain rate on stresses and strains recorded during the tests. Fig. 7 gives information on the surface and volume strain paths for the samples subjected to the 3D *ex situ* observations. From these figures, the following remarks can be made:

Stress–strain curves and surface aspects of samples – During constant strain rate tests, the *S* and *H* samples systematically exhibited an (elasto)viscoplastic response (Fig. 5a–b) with a sharp initial strain hardening until a stress peak σ_{max}, which was very similar for the two tested samples in Fig. 5a-b. After the stress peak, the

sample deformation exhibited softening until breakage. The breakage occurred at large tensile strains $\bar{\varepsilon}_{11}$ for the *S* samples (0.25 in the example of Fig. 5a), whereas the *H* samples always exhibited a less ductile behaviour with a failure at a lower strain (0.08 in Fig. 5b). This breakage was associated with the pull-out of fibre bundles from the impregnated network (Fig. 5a). For the ductile *S* samples, the morphologies of breakage zones also showed that during tensile tests, fibre bundles aligned along the tensile direction (see next subsection). Furthermore, regardless of the considered formulation, the tensile SMC behaviour drastically differed from its out-of-plane compression behaviour (Fig. 6a–b), where stress levels were approximately 1.5 (*S* samples) to 10 (*H* samples) times higher, and where no stress softening occurred. A weak anisotropy was also noted on tensile stress levels (Fig. 6b). Regardless of the investigated strain rate, the peak stress σ_{max} was approximately 1.2 times higher along the *MD* direction than along the *CD* direction for both formulations. This anisotropy effect could not be easily observed for the strains (see next point). At last, during the tests conducted with several constant strain rate loadings followed by stress relaxations, the tensile stress fully relaxed, as shown in the case of the *S* specimen in Fig. 4g.

Strain fields – Various interesting comments can be made from the strain measurements obtained using DIC and 3D imaging:

- As shown in the maps of the local strain field ε_{11} in Fig. 5a, two stages occurred during the sample deformation, regardless of the formulation and the strain rate. First, the 2D Hencky strain tensor **ε** was rather homogeneous and did not exhibit any shear component in $(\mathbf{e}_1, \mathbf{e}_2)$. This regime was obtained even after the nominal stress peak σ_{max}. Second, above a critical tensile strain $\bar{\varepsilon}_{crit}$, which was arbitrarily defined when the local strain field ε_{22} deviated from its mean value $\bar{\varepsilon}_{22}$ with a relative standard deviation (RSD) above 5% (Fig. 5b–c), the sample deformation was heterogeneous, showing localised deformation in the form of bands which spread over the sample width (the critical tensile strain $\bar{\varepsilon}_{crit}$ was close to 0.1 and 0.025 for the *S* and *H* specimens, respectively, as shown in Fig. 5b–c). In these bands, the strains were the highest. In addition, no well-defined inclination angle of the bands with respect to the tensile direction could be properly determined, ranging between 40° and 90°.
- Below the critical tensile strain $\bar{\varepsilon}_{crit}$, strain paths recorded during tests performed at constant strain rate (Fig. 4b–c) were practically linear, regardless of the considered formulation. Thus, for these conditions, the tangent transverse Poisson ratio $\nu_{12} = -\mathrm{d}\varepsilon_{22}/\mathrm{d}\varepsilon_{11} \approx -\bar{\varepsilon}_{22}/\bar{\varepsilon}_{11}$ was estimated. The Poisson ratio was close to 0.35 and 0.27 for the *S* and *H* samples, respectively. As shown in Fig. 6d, it was difficult to distinguish the values obtained along the *MD* and *CD* directions so that at first approximation $\nu_{CD} \approx \nu_{MD}$. The situation was more complex for the experiments performed with stress relaxation (Fig. 5e–f). Indeed, as illustrated in Fig. 5f, the strain paths were no more linear even below the critical strain. In particular, if the axial tensile strain $\bar{\varepsilon}_{11}$ remained constant during the relaxation, the transverse strain $\bar{\varepsilon}_{22}$ exhibited noticeable partial recovery.
- Using the 3D images of the *ex situ* tests, the mean surface ($\bar{\varepsilon}_s$) and volume ($\bar{\varepsilon}_v$) strains of the samples at various imposed tensile strains was assessed, as shown in Fig. 7. As proved in Fig. 7a, the mean surface strain deduced from the 3D images was nearly the same as that measured on the surface of the sample using DIC. Furthermore, this figure shows that the mean volume strain $\bar{\varepsilon}_v$ of the *S* sample was lower than the surface strain $\bar{\varepsilon}_s$, whereas these two strains were practically identical for the *H* sample. Below $\bar{\varepsilon}_{crit}$, the out-of-plane secant Poisson ratio $\bar{\nu}_{13}$ (between the undeformed initial configuration and the fully relaxed configuration) could be calculated, *i.e.*,
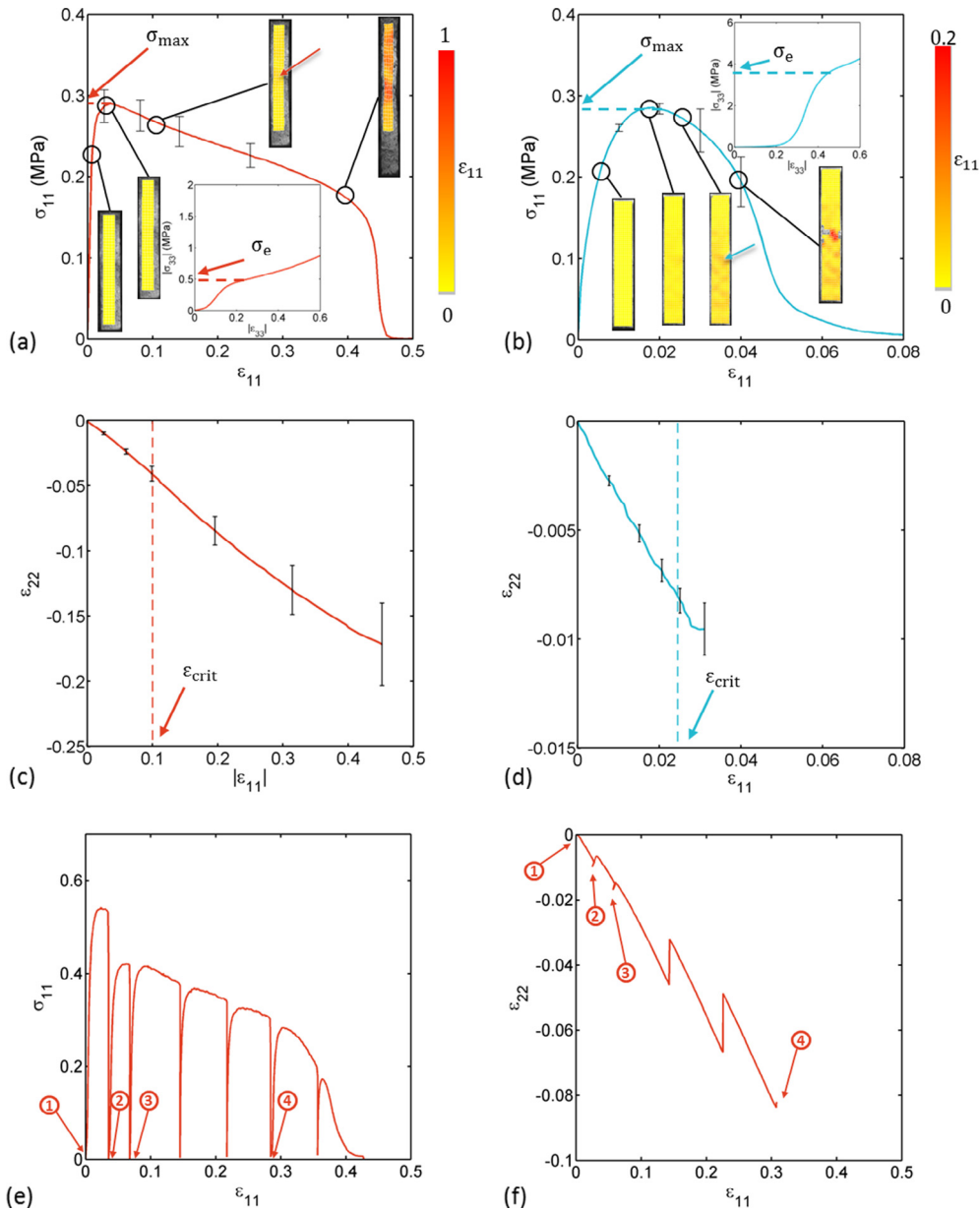
Fig. 5. Typical stress–strain curves (in a, b, e, the error bars represent the maximal deviation of the stress, the insets in a and b represent typical results obtained in transverse compression) and strain paths (in c, d, f, the error bars represent the standard deviation of ε_{22} on the surface of the samples) for the S (a, c, e, f) and H (b, d) formulations and for tests performed at constant strain rate of 10^{-3} s^{-1} (a, b, c, d) or with stress relaxations (e, f, the symbols ① to ④ indicate where the 3D images of the stretched sample were acquired). (For interpretation of the references to colour in this figure legend, the reader is referred to the web version of this article.)

$\bar{v}_{13} = (\bar{\varepsilon}_v - \bar{\varepsilon}_s)/\bar{\varepsilon}_{11}$. For the considered strain and strain rate history, and for the S and H samples, $\bar{v}_{13}$ was equal to averaged values of 0.3 an 0, respectively.

Influence of the strain rate and strain rate history – The tensile strain rate $\bar{D}_{11}$ and its history have a great effect on the tensile behaviour of SMCs:

– As clearly evidenced in Fig. 6b, for constant strain rate tests, the peak stresses σ_{max} were largely affected by the strain rate. They were slightly higher for the MD direction and much lower than the flow stress obtained in transverse compression (inset in the figure). In addition, below a tensile strain rate $\bar{D}_{11} = 1.10^3$ s^{-1}, the peak stresses of the H samples were slightly higher than those of S samples, this trend being reversed above this strain

rate. The peak stress followed a power-law function of the tensile strain rate $\bar{D}_{11}$, *i.e.*, $\sigma_{max} \approx \eta_0 \bar{D}_{11}^n$. Resulting values have been reported in Table 1. it is interesting to mention that the power-law exponent n is identical in tensions (MD or CD) and in transverse compression (regardless of the formulation) with $n = 0.44$ and 0.33 for the S and H formulation, respectively.

– As shown in Fig. 6a, c–d the tensile strain rate $\bar{D}_{11}$ also drastically affected the flow of the S specimens and, to a less extent, that of the H specimens. Fig. 6a shows that the lower the strain rate, the higher the SMC ductility. This point is quantitatively highlighted in Fig. 6c, showing that the critical strain $\bar{\varepsilon}_{crit}$ (i) was a decreasing function of $\bar{D}_{11}$, (ii) and reached very high values close to 1 for the S formulation at the lowest investigated strain rate. It is also worth mentioning that the strain rate
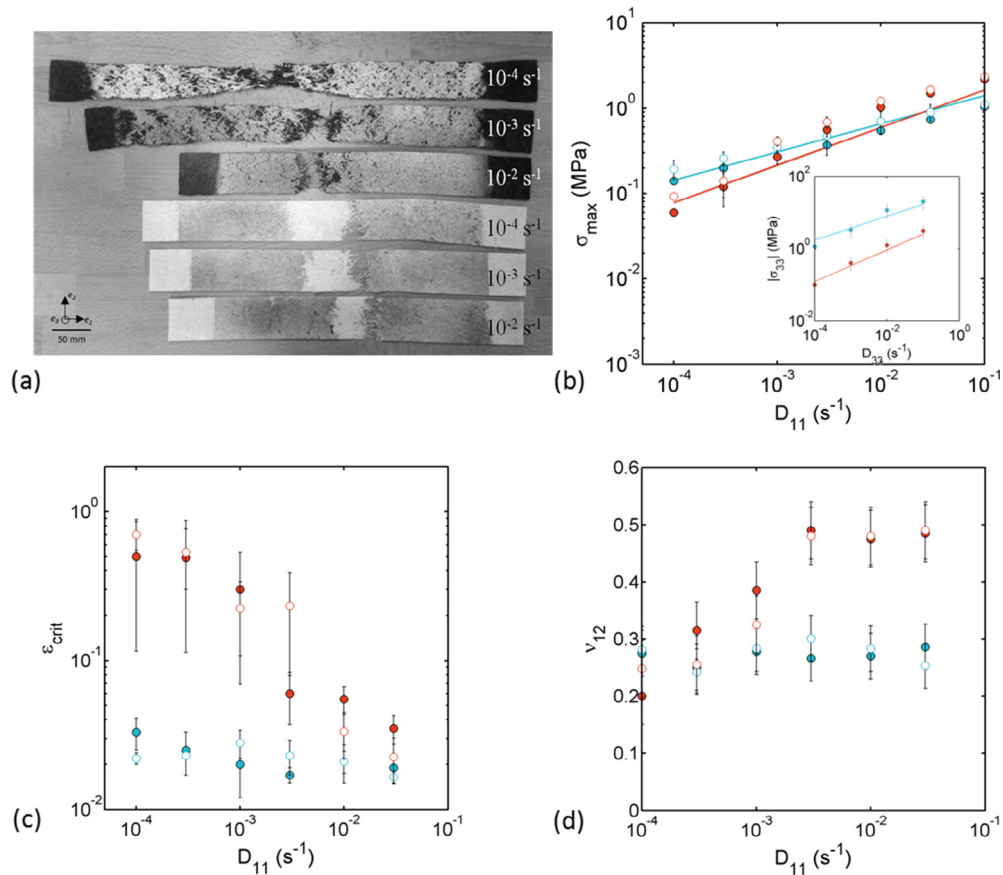
Fig. 6. (a) Photographs of the samples after tests performed at various constant strain rates. Evolution of (b) the peak stress σ_{max} (in tension) or the flow stress (in compression, inset), (c) the critical strain ε_{crit} and (d) the Poisson's ratio v_{12}, as a function of the applied strain rate. In the graphs, blue and red symbols are related to the *H* and *S* formulations, respectively, whereas open and filled symbols correspond to the *MD* and *CD*, respectively). (For interpretation of the references to colour in this figure legend, the reader is referred to the web version of this article.)
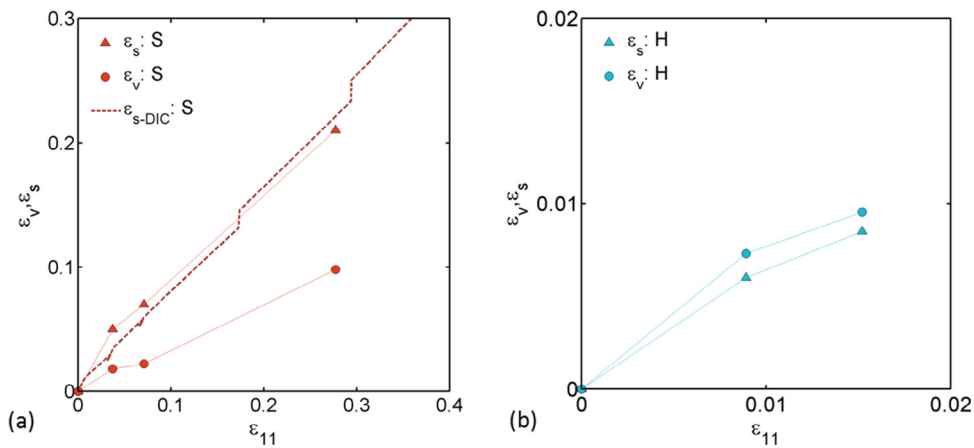
Fig. 7. Evolution of the volume ε_v and surface ε_s strains as a function of the tensile strain for the *S* (a) and *H* (b) formulations ($\bar{D}_{11} = 5.10^{-3}$ s^{-1}). In graph (a), the dashed line represents the surface strain that was obtained using DIC on the entire surface of the *S* sample. (For interpretation of the references to colour in this figure legend, the reader is referred to the web version of this article.)

history also affected the ductility of SMCs. Indeed, according to Fig. 6c, $\bar{\varepsilon}_{crit}$ was close to 0.04 for a constant strain rate of 5.10^3 s^{-1}, whereas a value of 0.06 was recorded for the test which results are shown in Fig. 5e–f and that were performed at the same strain rate but with multiple relaxation stages with a duration of $\approx$2 h. At last, Fig. 6d shows that the tensile strain rate $\bar{D}_{11}$ also altered the other components of the strain field $\boldsymbol{\varepsilon}$ of the *S* samples: the tangent Poisson function v_{12} recorded during

constant strain rate tests progressively increased from 0.25 to 0.5 above 3.10^3 s^{-1}. On the contrary, v_{12} was practically constant for the *H* specimens.

3.2. Initial and flow-induced microstructures

Results obtained from the 3D images of the *S* and *H* samples are shown in Figs. 8–10 and allow the initial and flow-induced

Table 1
Values of the consistency η_0 and the power-law exponent n used to fit experimental data shown in Fig. 6b with power-law functions.

Formulation	Loading	Direction	η_0 (MPa s^{-n})	n
S	Tension	MD	6	0.44
S	Tension	CD	4.8	0.44
H	Tension	MD	6	0.33
H	Tension	CD	2.5	0.33
S	Compression	–	6	0.44
H	Compression	–	36	0.44

microstructures of SMCs to be characterised. The following comments can be made:

*Porosity* – As it has been already reported in [20], the two studied SMC formulations exhibited a significant amount of pores in their initial configurations. The volume fraction of pores ϕ_{p0} for the S and H samples was equal to 0.047 and 0.33, respectively (Fig. 8a). These porosities were slightly higher than those reported in [20], as the samples analysed in the cited study were first subjected to a small pre-compaction that altered and decreased their initial porosities. It is also interesting to notice from the 2D porosity map in Fig. 9a that the volume fraction of pores was not perfectly homogeneous along the sample height (see the examples shown with the arrows): this is mainly ascribed to the process used to manufacture the sheets [1,35]. In addition, for both formulations, subjecting samples to a tensile strain led to a pronounced increase in the porosity (Fig. 8a): this is (i) in accordance with the evolution of the sample volume strain $\bar{\varepsilon}_\nu$ (Fig. 7), (ii) whereas an opposite trend was seen transverse compression [20]. Obvi-

ously, the porosity increase was much more pronounced for the ductile S samples which could be deformed to higher strains than the H samples. Lastly, it is worth noticing that the initial macroscale pore gradients were enhanced during tensile tests (Fig. 9). This figure also shows that zones with initially higher porosity corresponded to zones where the strain field localised upon stretching the samples.

Pore anisotropy – In accordance with the previously reported results [20], Fig. 8b shows that the pores inside the two SMC formulations exhibited transverse isotropy, with $r_{12} < r_{13} \approx r_{23}$ (values reported in [20] for r_{13} and r_{23} are slightly higher than those shown in the graph due to the sample precompaction): pores were flat and lay in the ($\mathbf{e}_1$, $\mathbf{e}_2$) plane, most of them being closed (resp. open) for the S (resp. H) sample [20]. During stretching, pores still remained flat but two tendencies occurred for both formulations: (i) the pore transverse isotropy evolved towards a more general anisotropy, *i.e.*, $r_{12} \neq r_{13} \neq r_{23}$, (ii) the anisotropy magnitude increased (all anisotropy ratios increased). These trends differed
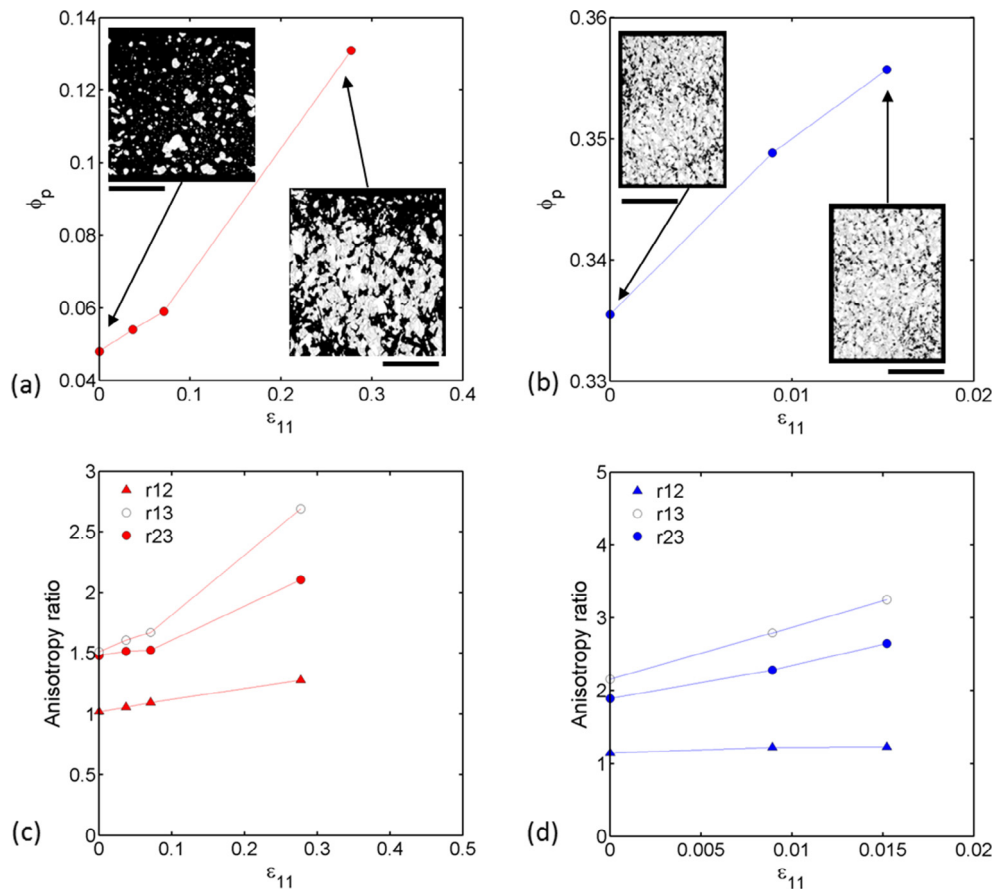
Fig. 8. Evolution of the porosity ϕ_p (a–b) and the pore anisotropy ratios r_{12}, r_{13}, r_{23} (c–d) as a function of the tensile strain $\bar{\varepsilon}_{11}$ for the S (a, c) and H (b, d) formulations. The inset graphs (a) and (b) correspond to the 3D upper views of the porous phase (the scale bar represents 1 mm). (For interpretation of the references to colour in this figure legend, the reader is referred to the web version of this article.)
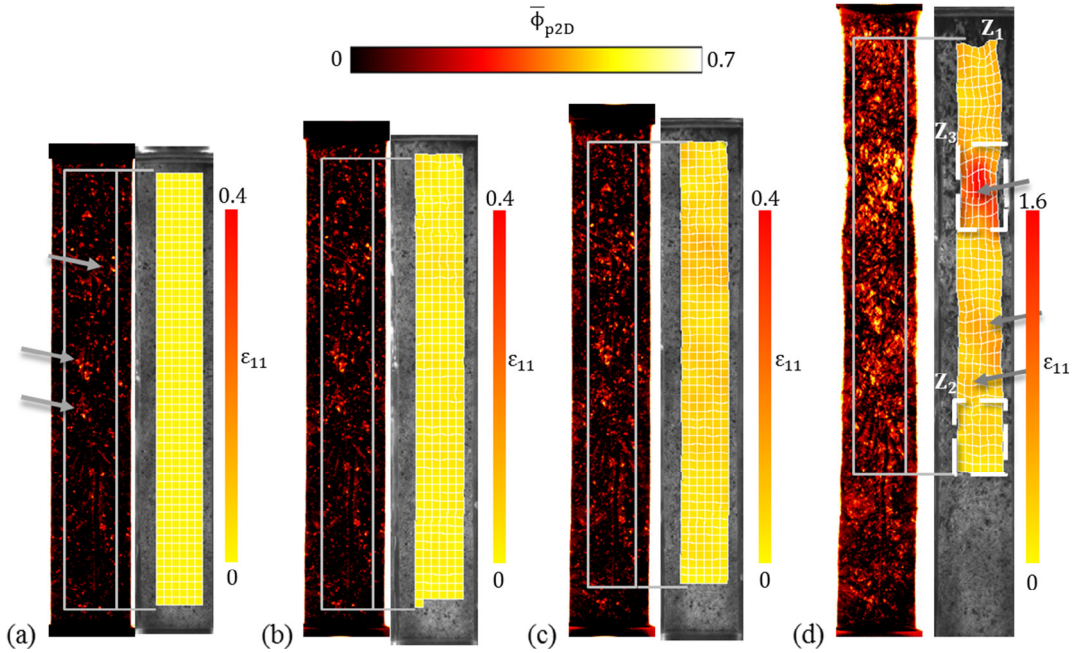
Fig. 9. 2D maps that show the porosity averaged along the thickness $\bar{\phi}_{p2D}$ of the S sample subjected to the *ex situ* test and corresponding 2D strain fields ε_{11} at various compressive strains $\bar{\varepsilon}_{11}$: (a) 0, (b) 0.006, (c) 0.09, (d) 0.28 for the S sample. In (d), Z_i correspond to the zones that were used to build Fig. 8. (For interpretation of the references to colour in this figure legend, the reader is referred to the web version of this article.)
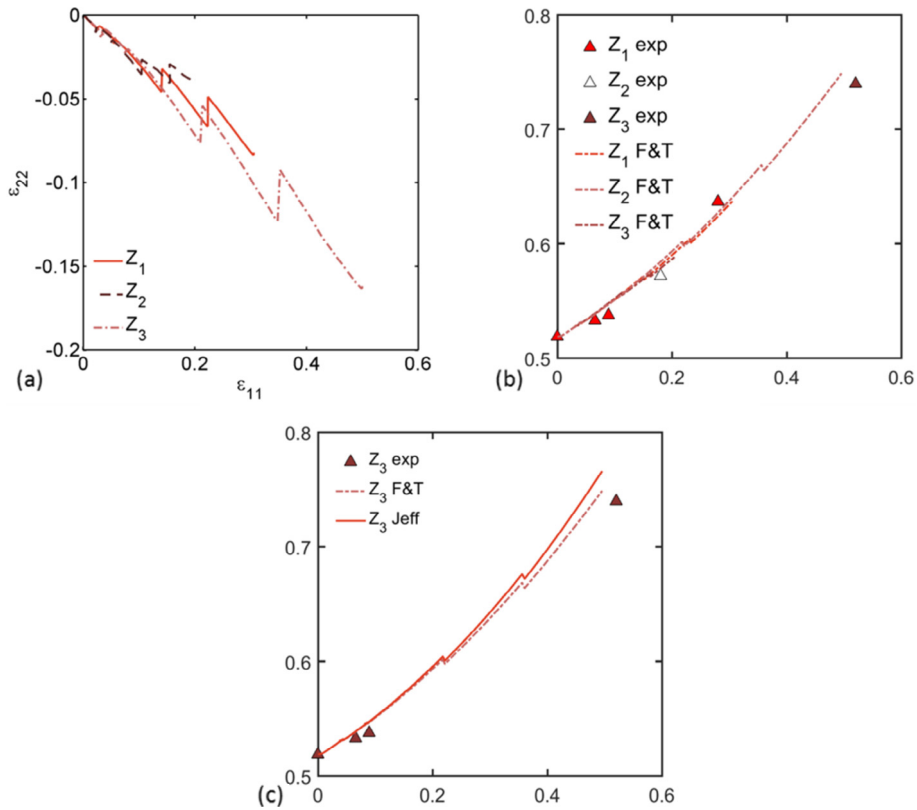
Fig. 10. (a): surface strain paths in the zones Z_i shown in Fig. 7d (a). (b): measured (marks) and predicted (lines, using Eq. (3) with $C_i = 0.02$) values of the component A_{11} of the second order fibre bundle orientation tensor **A** for the three zones. (c) For zone Z_3, comparison between the experimental values (marks) and those given by Eq. (3) with $C_i = 0$ (continuous line) and $C_i = 0.02$. (dashed-dotted line). (For interpretation of the references to colour in this figure legend, the reader is referred to the web version of this article.)

from those recorded during transverse compression, during which pores kept their transversely isotropic shape and became more and more isotropic with the compression [20].

Fibre bundle orientation – In their initial configuration, both formulations practically exhibited planar random fibre bundle orientation, with a weak alignment along the *MD* direction probably induced by the sheet manufacturing process. For the imaged *S* and *H* samples, the corresponding second order fibre bundle orientation tensors in the whole samples were very close and were expressed as follows (the *MD* is parallel to the tensile axis $\mathbf{e}_1$):

$$\mathbf{A} \approx \begin{bmatrix} 0.52 & \approx 0.00 \\ \approx 0.00 & 0.48 \end{bmatrix}_{\mathbf{e}_1,\mathbf{e}_2} \tag{2}$$

As illustrated in Fig. 10b, it was possible to follow the evolution of $\mathbf{A}$ for the *S* sample during stretching (because of the small strains obtained with the *H* specimen, the method was not sensitive enough to capture any significant orientation change). In this figure, only the component A_{11} of $\mathbf{A}$ was reported since the non-diagonal components $A_{12} = A_{21}$ were weak and since $A_{22} = 1 - A_{11}$. Three estimations were done. The first one corresponded to the entire correlation grid denoted Z_1 in Fig. 9. The two others were obtained in smaller correlation zones shown in Fig. 9d, *i.e.*, in subzones where the strain field remained homogenous (denoted Z_2 in the figure) or exhibited strain localisation (denoted Z_3) during stretching, respectively. The three strain paths of these zones are plotted in Fig. 10a, showing both strain recovery effects as well as the large differences between them. Fig. 10b shows that, regardless of the considered zone, fibre bundles aligned along the stretching direction $\mathbf{e}_1$. Furthermore, the higher the tensile strain in the considered zone, the higher the fibre bundle alignment. In addition, important orientation difference appeared between all zones: in zone Z_1, $\bar{\varepsilon}_{11} = 0.3$ and $A_{11} \approx 0.65$, whereas $A_{11} \approx 0.75$ in subzone Z_3 where strain localised and $A_{11} \approx 0.55$ in subzone Z_2 within which $\bar{\varepsilon}_{11} = 0.25$.

4. Discussion

The two SMC formulations tested in this study had rather different microstructures. The *S* specimens had a low initial pore content with closed pores, whereas the *H* specimens had a high amount of pores which were mainly open [20]. In addition, the matrix of *H* samples mainly impregnated the fibre bundles or formed joints in contact zones between fibre bundles. These different microstructures led to two tensile mechanical behaviours:

– The first difference was revealed from stress levels, which were surprisingly of the same order of magnitude, despite the higher fibre content in the *H* specimens. This is mainly related to the high pore content in the *H* samples. Indeed, standard SMCs are usually considered to be highly concentrated fibre suspensions, within which two main micro-deformation mechanisms contribute to the their overall stress tensors [5,40]: elastoviscoplastic friction forces occurring at the numerous bundle-bundle contacts and short-range elastoviscoplastic interactions of the matrix with fibre bundles away from contact zones. Obviously, the *H* samples rather resemble to porous media than to fibre suspensions, so that the last contribution could be neglected due to the very high pore content. On the contrary, it played a role on the overall tensile stress response of the *S* samples which can still be viewed as concentrated suspensions. Thus, the fibre–matrix interaction could be seen as an additional stress contribution that would make stress levels reach those exhibited by the *H* samples.

– The second difference was related to the macroscale post-peak deformation modes which depended on the considered formulations (Fig. 5), *i.e.*, with a pronounced ductile response for the *S* formulation and a much less ductile flow for the *H* formulation. Once again, the high (resp. low) pore contents of the *H* (resp. *S*) formulations may be responsible. Indeed, during the flow of *H* specimens, polymer bundle-bundle bonds were highly sheared and could be irreversibly broken and not rejuvenated elsewhere as there was practically no polymer matrix elsewhere in the SMCs [20]. On the contrary, when bonds broke in the *S* specimens, they could be rejuvenated elsewhere due to the presence of the matrix surrounding the fibre bundles. However, these effects could be restrained by the increase in the strain rate (Fig.6a). From a practical standpoint, it is thus important to restrain the initial pore content in SMCs and the tensile strain rate they are subjected to in order to increase their ductility during stamping or moulding flow phases.

In parallel, some features of the tensile behaviour of the *S* and *H* samples were similar. They are detailed below and discussed in regards to those obtained for other fibrous materials with comparable disordered planar fibrous networks.

– SMCs exhibited an elastoviscoplastic behaviour with strain hardening, softening and damage up to failure, as reported for papers or non-woven materials [25,32,34,41–43]. However, due the viscous nature of the matrix surrounding the fibre bundles and to the weak fibre bundle entanglement, the tensile behaviour of SMCs rather resembled to that of fluids rather than to solids, as these materials exhibited (i) a pronounced strain rate sensitivity (this behaviour is less pronounced for dry papers and non-wovens) and (ii) practically full stress relaxation when stopping the strain loading (Fig. 5). In addition, it is interesting to mention that for the two tested formulations, the strain rate sensitivity did not depend on the orientation of the samples (*MD* or *CD*), nor on the type of loading (in-plane tension or out-of-plane compression): given the SMC formulation, the power-law exponent n remained unchanged (Fig.6b, Table 1), as it has already been reported for other SMC formulations [16,17]. This point is interesting as it validates this assumption made in many SMC rheological models.

– SMCs dilated as paper materials and other soft fibrous materials upon stretching. This phenomenon is related to the mechanics of their fibrous network and to the interaction of fibre bundles with the matrix. This induced the increase in their porosity (Fig. 8). At low strain rates, *i.e.*, when viscous effects induced in the matrix were weak, it is interesting to mention that both formulations exhibited an in-plane tangent Poisson ratio ν_{12} of approximately 0.27. This value is very close to those that have often been reported for paper materials with planar random fibre orientation [44]. The comparison is even still valid at higher strain rates for the *H* formulation, the microstructure of which is closer to that of papers. For the imaged *H* sample, the out-of-plane secant Poisson ration ν_{13} was close to 0, in accordance with data reported for several paper materials too [41].

– As for papers or nonwoven materials, the SMC manufacturing [1] induced several microstructure features and defects that altered their tensile properties. For example, an initial weak fibre alignment was induced in the SMCs which led to their weakly orthotropic mechanical behaviour. Furthermore, the sheet manufacturing also induced noticeable gradients for the spatial distribution of fibre bundles within the sheets, in the form of flocs or aggregates (Fig. 9) [35]. As for paper materials

or nonwoven sheets, for which similar heterogeneities are generated during their manufacturing [27,28,33], undesirable strain localisation bands were also observed in low fibre content zones (Fig. 9) and induced an important decrease in the ductility of the SMC samples. Thus, it is clear that minimising the fibre content gradients in the sheets during their manufacturing would greatly improve their formability during stamping or compression moulding.

– For several aspects, the in-plane stretching behaviour of the two tested SMCs significantly differed from that obtained during transverse compression. This is mainly related to the presence of positive (in tension) or negative (in compression) isostatic stresses. During transverse compression, negative isostatic stresses occurred so that pores disappeared and the fibre bundle networks was consolidated, storing bending and contact elastic energies [20,45]. This led to noticeable strain-hardening which is clearly apparent in the stress–strain curves and to stress levels much higher than in tension (Fig. 5). On the contrary, for tension, *i.e.*, with a positive isostatic stress, SMCs dilated, leading to a progressive increase in the porosity and damage of the bonds between fibre bundles, and thus to a softening of the stress–strain curves which led to the breakage of samples. Such a strong tension–compression asymmetry and, more generally the effects of isostatic pressure on the SMC volume variations are unfortunately not properly taken into account in current SMC rheological models. Most of them assume the SMC incompressibility, and thus cannot account for the observed pronounced pressure induced volume or porosity variations. Besides, none of them accounts for sample breakage above a pressure dependent strain state.

– During stretching, fibre bundle aligned along the tensile direction, as it has already been observed for non-woven fabrics or other soft fibrous materials [25,26,32]. Combined with the sample stretching, this alignment also caused pores to take a slender shape (Fig. 7). We checked whether the observed evolution of the fibre bundle orientation could be predicted by the Jeffery's equation [46] modified by Folgar and Tucker for concentrated suspensions [47]. This equation was written assuming fibre bundles as slender rods, lying in the $(\mathbf{e}_1, \mathbf{e}_2)$ plane:

$$\frac{\mathrm{D}}{\mathrm{D}t}\mathbf{A} = \mathbf{L} \cdot \mathbf{A} - \mathbb{A} : \mathbf{D} + 2C_i|\dot{\gamma}|(\boldsymbol{\delta} - 3\mathbf{A}), \tag{3}$$

where $\mathbf{L}$ is the velocity gradient, $\dot{\gamma} = \sqrt{\mathbf{D} : \mathbf{D}}$ the generalised shear rate, $\mathbb{A}$ the fourth-order fibre bundle orientation tensor [37], $\boldsymbol{\delta}$ the identity tensor and where C_i is the Folgar and Tucker constant used to account for fibre–fibre interactions during the SMC flow. The prediction of this equation was compared to the fibre bundle orientation evolution measured during the *ex situ* test performed with of the S sample (Fig. 10b). This comparison was achieved for the three zones Z_i shown in Fig. 9. For that, the time integration of Eq. (3) was performed using a fourth-order Runge Kunta scheme implemented in Matlab, and the velocity gradients $\mathbf{L}$, as well as the strain rate tensors $\mathbf{D}$ were derived from DIC measurements that led to the three strain paths plotted in Fig. 10a. Furthermore, the orientation tensor $\mathbb{A}$ was estimated using the hybrid closure approximation from the knowledge of $\mathbf{A}$ [37]. Lastly, the interaction coefficient C_i was determined to obtain the best fits of the three assessed experimental evolutions, leading to a value of 0.02 which is rather close to those found for short fibre-reinforced polymer composites [47,48]. Results are reported in Fig. 10b showing good prediction of the modified Jeffery's equation for the three strain paths. Thus, even if the modified Jeffery's equation was initially written for incompressible fibre suspensions, it is interesting to notice from Fig. 10b that it could however represent the experimental trends in the three

considered zones Z_i. This is interesting as (i) the recorded strain paths were very complex and exhibited viscoelastic strain recoveries (Fig. 10a) and compressible trajectories (Fig. 7a). In addition, we have also plotted in Fig. 10c the prediction of the modified and the non-modified ($C_i = 0$) Jeffery's equation for zone Z_3, showing that the non-modified equation provides a faster fibre re-orientation, but still fairly in good accordance with the experimental measurements.

5. Conclusion

An important experimental database was obtained in this study to characterise and better understand the in-plane tensile rheology of two uncured SMCs with different microstructures. In particular, thanks to (i) the measurement of the local kinematical fields on the surface of stretched samples (DIC method) and (ii) the 3D imaging of their flowing microstructures (*ex situ* X-ray microtomography), interesting observations and results could be obtained. They are summarised in the following points:

– Over a wide range of in-plane tensile strain rates, SMCs exhibited a fluid-like behaviour with (i) shear thinning effects that were identical to those observed in transverse compression, (ii) strain-hardening followed by softening, damage and breakage. These three last features are different from those observed during transverse compression and not taken into account into current SMC rheological models although they often occur during the flowing phases of the compression moulding process, inducing undesirable defects (Fig. 1).

– Upon stretching, SMCs exhibited positive volume variation. Initial pores contained in SMCs grew and took slender shapes parallel to the tensile direction, whereas the two opposite trends were observed during transverse compression. For low initial pore content, the volume variation was progressively restrained by the presence of the matrix, and the ductility of sample reached substantial values. On the contrary, for high initial pore contents, the porosity rapidly increased yielding to a fast sample breakage. To date, no constitutive theory accounts for the presence of pores and for the effect of the isostatic stress on their growth in SMC rheological models. Combined with the results obtained previously in transverse compression with the same SMC formulations [20], the database gained here will be useful to build rheological compressive models with relevant pore growth kinetics.

– Meanwhile, fibre bundles aligned along the stretching direction, following rotational kinematics rather well described by the (non-)modified Jeffery's equation, even if SMCs were compressible media.

– The tensile SMC ductility, and thus the capacity of these materials to be stamped or stretched during compression moulding, depended on the loading condition and on their initial microstructure. In particular, it depended on the stretching rate, the SMC ductility being more important at lower strain rates.

– In addition, two principal microstructure features were identified as playing leading and negative roles on the SMC ductility. Both of them should be better controlled and minimised during the fabrication of the prepregs. The first parameter is the initial porosity contained in the sheets: as shown in the case of the high fibre content formulation, large initial pore content does not allow bundle-bundle bonds to be repaired or rebuilt/rejuvenated during stretching, leading to rapid damage and breakage of the sheets that exhibits a low ductility. As already been pointed out in [20], optimising the impregnation of the fibre bundle mats during the calendering phase during the manufacturing of the sheets could reduce the initial pore content. The

second parameter is the spatial distribution of fibre bundles within the sheets: regardless of the SMC formulation, flocs or aggregates of fibre bundles led to early strain localisation bands in stretched samples, thus limiting drastically their overall ductility. Thus, it could be very interesting to minimise the formation of flocs during the sheet fabrication.

Acknowledgements

References

[1] Orgéas L, Dumont PJJ. Sheet molding compounds. In: Wiley Encycl Compos. Wiley; 2012. p. 2683–718.

[2] Abrams L, Castro JM, Boylan S. Predicting molding forces during sheet molding compound (SMC) compression molding. II: Effect of SMC composition. Polymer 2003;24:731–47.

[3] Osswald TA, Davis BA, Gramann PJ, Rios A. Compression molding. Munich: Hanser Publishers; 2003.

[4] Lee LJ. Curing of compression molded sheet molding compound. Polym Eng Sci 1981;21:483–92.

[5] Guiraud O, Dumont PJJ, Orgéas L, Favier D. Rheometry of compression moulded fibre-reinforced polymer composites: rheology, compressibility, and friction forces with mould surfaces. Compos Part A-Appl S 2012;43:2107–9.

[6] Odenberger PT, Andersson HM, Lundström TS. Experimental flow-front visualisation in compression moulding of SMC. Compos Part A-Appl S 2004;35:1125–34.

[7] Barone MR, Caulk DA. Kinematics of flow in sheet molding compounds. Polym Compos 1985;6:105–9.

[8] Olsson NEJ, Lundström TS, Olofsson K. Design of experiment study of compression moulding of SMC. Plast Rubber Compos 2009;38:426–31.

[9] Marker LF, Ford B. Flow and curing behaviour of SMC during molding. Mod Plast 1977:64–70.

[10] Lee LJ, Marker LF, Griffith RM. The rheology and mold flow of polyester sheet molding compound. Polym Compos 1981;2:209–18.

[11] Michaeli W, Mahlke M, Osswald TA, Nolke M. Simulation of the Flow in SMC. Kunststoffe Ger Plast 1990;80:31–3.

[12] Kim KT, Jeong JH, Im YT. Effect of molding parameters on compression molded sheet molding compounds parts. J Mater Process Technol 1997;67:105–11.

[13] Kim J, Shiau YC, Lee LJ, Im YT. Compression molding simulation of chopped fiber reinforced polymeric composites in plate-rib type geometry. Polym Compos 1992;13:97–107.

[14] Lin CM, Weng CI, Ho CT. Anisotropy in sheet molding compounds during compression molding. Polym Compos 1997;18:613–22.

[15] Lin CM, Weng CI. Simulation of compression molding for Sheet Molding Compound considering the anisotropic effect. Polym Compos 1999;20:98–113.

[16] Dumont PJJ, Orgéas L, Le Corre S, Favier D, Le Corre S. Anisotropic viscous behaviour of Sheet Molding Compounds (SMC) during compression molding. Int J Plast 2003;19:625–46.

[17] Le Corre S, Orgéas L, Favier D, Tourabi A, Maazouz A, Venet C. Shear and compression behaviour of sheet moulding compounds. Compos Sci Technol 2002;62:571–7.

[18] Kotsikos G, Gibson AG. Investigation of the squeeze flow behaviour of Sheet Moulding Compounds (SMC). Compos Part A-Appl S 1998;29:1569–77.

[19] De La Caba K, Guerrero P, Eceiza A, Mondragon I. Kinetic and rheological studies of two unsaturated polyester resins cured at different temperatures. Eur Polym J 1997;33:19–23.

[20] Ferré Sentis D, Orgéas L, Dumont PJJ, Rolland du Roscoat S, Sager M, Latil P. 3D in situ observations of the compressibility and pore transport in Sheet Moulding Compounds during the early stages of compression moulding. Compos Part A-Appl S 2017;92:51–61.

[21] Launay J, Hivet G, Duong A, Boisse P. Experimental analysis of the influence of tensions on in plane shear behaviour of woven composite reinforcements. Compos Sci Technol 2008;68:506–15.

[22] Lee W, Padvoiskis J, Cao J, De Luycker E, Boisse P, Morestin F, et al. Bias-extension of woven composite fabrics. Int J Mater Form 2008;1:185–8.

[23] Vanleeuw B, Carvelli V, Barburski M, Lomov SV, Van Vuure AW. Quasi-unidirectional flax composite reinforcement: Deformability and complex shape forming. Compos Sci Technol 2015;110:76–86.

[24] Vacher P, Morestin F, Dumoulin S, Mgil-Touchal S. Bidimensional strain measurement using digital images. In: IMECHE editor. Proc Inst Mech Eng Part C J Mech Eng Sci, 1999, p. 811–7.

[25] Kabla A, Mahadevan L. Nonlinear mechanics of soft fibrous networks. J R Soc Interface 2007;4:99–106.

[26] Rodney D, Gadot B, Rui Martinez O, Rolland S, Orgéas L. Reversible dilatancy in entangled single-wire materials. Nat Mater 2016;15:72–8.

[27] Wong L, Kortshot MT, Dodson CTJ. Effect of formation on local strain fields and fracture of paper. J Pulp Pap Sci 1996;22:213–9.

[28] Considine JM, Scott CT, Gleisner R, Zhu JY. Use of digital image correlation to study the local deformation field of paper and paperboard. In: 13th Fundam Res Symp, 2005, p. 613–0.

[29] Isaksson P, Dumont PJJ, Rolland Du Roscoat S. Crack growth in planar elastic fiber materials. Int J Solids Struct 2012;49:1900–7.

[30] Poquillon D, Viguier B, Andrieu E. Experimental data about mechanical behaviour during compression tests for various matted fibres. J Mater Sci 2005;40:5963–70.

[31] Viguié J, Dumont PJJ, Orgéas L, Vacher P, Desloges I, Mauret E. Surface stress and strain fields on compressed panels of corrugated board boxes. An experimental analysis by using Digital Image Stereocorrelation. Compos Struct 2011;93:2861–73.

[32] Jubera R, Ridruejo A, González C, Llorca J. Mechanical behavior and deformation micromechanisms of polypropylene nonwoven fabrics as a function of temperature and strain rate. Mech Mater 2014;74:14–25.

[33] Ridruejo A, González C, Llorca J. Micromechanisms of deformation and fracture of polypropylene nonwoven fabrics. Int J Solids Struct 2011;48:153–62.

[34] Rawal A, Lomov S, Verpoest I. An environmental scanning electron microscope study of a through-air bonded structure under tensile loading. J Text I 2008;99:235–41.

[35] Guiraud O, Dumont PJJ, Orgéas L. How to prepare SMC and BMC-like compounds to perform relevant rheological experiments? Appl Compos Mater 2013;20:157–69.

[36] Rezakhaniha R, Agianniotis A, Schrauwen JTC, Griffa A, Sage D, Bouten CVC, et al. Experimental investigation of collagen waviness and orientation in the arterial adventitia using confocal laser scanning microscopy. Biomech Model Mechanobiol 2012;11:461–73.

[37] Advani SG, Tucker CL. The use of tensors to describe and predict fiber orientation in short fiber composites. J Rheol 1987;3:751–84.

[38] Dumont PJJ, Vassal JP, Orgéas L, Michaud V, Favier D, Månson JAE. Processing, characterization and rheology of transparent concentrated fibre bundle suspensions. Rheol Acta 2007;46:639–51.

[39] Le TH, Dumont PJJ, Orgéas L, Favier D, Salvo L, Boller E. X-ray phase contrast microtomography for the analysis of the fibrous microstructure of SMC composites. Compos Part A-Appl S 2008;39:91–103.

[40] Orgéas L, Dumont PJJ, Le Corre S. Rheology of highly concentrated fiber suspensions. In: Chinesta G, Ausias F, editors. Rheol Non-Spherical Part Suspens, 2015, p. 119–66.

[41] Stenberg N, Fellers C. Out-of-plane Poisson's ratios of paper and paperboard. Nord Pulp Pap Res J 2002;17:387–94.

[42] Gurav SP, Bereznitski A, Heidweiller A, Kandachar PV. Mechanical properties of paper-pulp packaging. Compos Sci Technol 2003;63:1325–34.

[43] Hagman A, Nygårds M. Investigation of sample-size effects on in-plane tensile testing of paperboard. Nord Pulp Pap Res J 2012;27:295–304.

[44] Schulgasser K. The in-plane poisson ratio of paper. Fibre Sci Technol 1983;19:297–309.

[45] Toll S. Packing mechanics of fiber reinforcements. Polym Eng Sci 1998;38:1337–50.

[46] Jeffery GB. The motion of ellipsoidal particles immersed in a viscous fluid. In: Proc Roy Soc London, 1922, p. 161–79.

[47] Folgar F, Tucker III CL. Orientation behavior of fibers in concentrated suspensions. J Reinf Plastics Compos 1984;3:98–119.

[48] Bay RS. Fiber orientation in injection molded composites: a comparison of theory and experiments PhD Thesis. USA: Univ. Illinois; 1991.